THE ASTROPHYSICAL JOURNAL, 406:112–121, 1993 March 20

NEAR-INFRARED IMAGING OF THE BECKLIN-NEUGEBAUER–IRc2 REGION IN ORION WITH SUBARCSECOND RESOLUTION

C. DOUGADOS AND P. LÉNA
Observatoire de Paris et Université Paris VII, 92195 Meudon, France; and Five College Astronomy Department, University of Massachusetts, Amherst

AND

S. T. RIDGWAY, J. C. CHRISTOU, AND R. G. PROBST
Kitt Peak National Observatory,[1] P.O. Box 26732, Tucson, AZ 85726
Received 1992 June 2; accepted 1992 September 24

ABSTRACT

The Becklin-Neugebauer source has been partially resolved by speckle imagery at 3.6 μm with an angular resolution of 0".2. The images, fluxes, and additional constraints are consistent with a spherical dust shell of inner diameter 0".1, surrounding a hot star. The surrounding region, including the vicinity of IRc2, has been imaged with short-exposure/deconvolution methods at several wavelengths, at a resolution of 0".5. IRc2 is resolved into four components, and the fluxes of the detected sources were determined at 2.8 and 4 μm. Accurate astronomy of the infrared sources with respect to the SiO maser emission has been obtained. The centroid of the SiO maser is definitely not located at the center of symmetry between lobes A and B, but may correspond to IRc2 component A. Component B may arise in scattering from one lobe of a bipolar flow from source A, but other explanations are still possible. The multiple structure of the IRc2 source, the new limits on the size of the components, and the positional correlations draw into question the previous hypothesis that a single, very luminous source dominates the energetics of the BN-KL nebula.

Subject headings: infrared: interstellar: continuum — ISM: individual (Becklin-Neugebauer) — masers — techniques: interferometric

1. INTRODUCTION

The complexity of the Orion region in the Becklin-Neugebauer–Kleinmann-Low nebula has become increasingly apparent with the discovery of high-velocity molecular flow originating at or near IRc2 (Downes et al. 1981) and its detailed fine structure (Martín-Pintado, Rodríguez-Franco, & Bachiller 1990), the central role of IRc2 in the heating (Chelli, Perrier, & Léna 1984) and dynamics of the whole region, the complex radio structure at or near IRc2 involving SiO masers (Wright et al. 1990; Plambeck, Wright, & Carlstrom 1990), continuum emission (Churchwell et al. 1987; Garay, Moran, & Reid 1987), and H_2O masers (Garay, Moran, & Haschick 1989), as well as the ejection of Herbig-Haro objects moving away from the IRc2 region (Jones & Walker 1985). These led to the picture of IRc2 as a bright ($\approx 10^5\ L_\odot$) source which provides most of the luminosity reradiated by the BN-KL nebula in the mid- and far-infrared (Wynn-Williams et al. 1984). A doughnut-shaped or toroidal structure has been proposed to explain the SiO maser configuration (Wright & Plambeck 1983; Plambeck et al. 1990). The shape of IRc2 and its apparent spatial coincidence with the SiO maser suggested an association of the IR source with this structure (Chelli et al. 1984; Lester et al. 1985), which could collimate the flow along its polar axis and be located within a cavity, as suggested by the infrared polarization (Werner, Dinerstein, & Capps 1983; Wynn-Williams et al. 1984; Minchin et al. 1991) and by the flow discovered in NH_3 (Migenes et al. 1989). However, Gezari (1992) found that at 8–12 μm the peak of IRc2 is not coincident with the SiO maser position. The connection between IRc2 and neighboring sources is not clear.

The BN object itself, identified as a highly obscured early-type star (Foy et al. 1979), has shown a complex environment (Scoville et al. 1983).

In this paper we present near-infrared observations with a resolution reaching the diffraction limit of a 3.8 m telescope and extending previous work (Chelli et al. 1984), giving further insight into the subarcsecond structure of BN and IRc2.

2. THE OBSERVATIONAL TECHNIQUE

The data were obtained during two runs (1989 November and 1990 November) on the Kitt Peak 4 m Mayall telescope, using the 58 × 62 NOAO IR speckle camera (Beckers et al. 1988), equipped with the standard filters K (2.2 μm), L (3.6 μm), L' (3.8 μm), L'' (4 μm), M (5 μm), and a linear wire-grid polarizer. As astrometric accuracy is required, plate scale and orientation were calibrated on the double stars γ Leo and γ Ari, of known orbital parameters. Both stars were independently measured at Flagstaff Observatory (Dahn 1990) to provide accurate separations and position angles.

Using several image scales and sampling, we combine classical imaging with high-resolution techniques such as shift-and-add image restoration and speckle holography in natural and polarized light. We first observed the BN object at 3.6 μm in speckle mode using a pixel sampling of 0".048, in order to reach diffraction-limited information. We then obtained wider field maps at L', L'', and M and a polarimetric map at L'. Short exposures with pixel size 0".25 achieve proper sampling at M but slight undersampling at the two shorter wavelengths. Individual frames are mean-sky–subtracted and flat-fielded, then either re-centered frame by frame and co-added (*shift-and-add*) or deconvolved using *speckle holography*. In the latter case, an instantaneous point-spread function (PSF) is estimated by considering the core of BN as unresolved at the lower pixel sam-

[1] National Optical Astronomy Observatories, operated by the Association of Universities for Research in Astronomy, Inc., under cooperative agreement with the National Science Foundation.

pling (this is justified by our speckle data). Assuming isoplanicity over the field (~15″ width), the images are deconvolved frame by frame, with the instantaneous PSF, averaging to get the final image. Apodization is applied in order to control the restored PSF. Isoplanicity is a reasonable assumption over our images, as the isoplanatic field has been demonstrated to extend to more than 20″ at K for moderately good seeing (Rigaut et al. 1991).

3. THE STRUCTURE OF THE BN SHELL

3.1. *Data Analysis*

The BN object and its point-source comparison SAO 123067 were observed at 3.6 μm with a pixel sampling of 0″.048, and an exposure time of 0.05 s at an air mass of 1.4. The image scale has ~5% accuracy and ~2° uncertainty in field rotation. The data were taken in blocks of 500 frames and totaled 2000 frames of the point-source reference, 1500 frames of the program object, and 1500 sky frames. Of these, 1234 frames were selected for the program object and 1834 frames for the point-source reference after omission of frames whose speckle clouds overflowed the edge of the detector. The mean sky was subtracted from each frame before processing and was also used as the flat field. The data were reduced using the Knox-Thompson cross-spectrum algorithm in use at KPNO for the reduction of speckle interferometric data. This provides both the Fourier amplitudes and phases of the object after the point-source calibration. A detailed description of the reduction procedure is given by Christou (1991). Each of three object data sets was reduced separately using the adjacent point-source data for the seeing calibration. For spatial frequencies $f > 1.2$ cycles arcsec^{-1} the three curves are very similar. They differ substantially at the lower spatial frequencies which are dominated by seeing statistics. This difference is typical of the effects of seeing differences between the program object and the point source. Since there are insufficient frames for a binning procedure, the three independent results were averaged after normalizing the visibilities for $f > 1.2$ cycles arcsec^{-1}. The normalization factors were obtained from the level region of the ratios of the second and third data sets with the first, i.e., for $f > 1.2$ cycles arcsec^{-1}. The azimuthal average as well as the cuts at 0° and 90° are displayed in Figure 1. The error bars represent the standard errors of the means.

3.2. *Results*

The source is clearly resolved with the visibility dropping to ~70% at 5.5 cycles arcsec^{-1}. There is no obvious decomposition of the visibility into a resolved structure, i.e., a shell, and an unresolved stellar component. In order to make such a distinction, greater spatial frequency coverage would be required. However, using simplistic models, preliminary estimates were obtained for the object structure assuming two extremes. The first assumed only a Gaussian shell component, and the second also assumed an unresolved component with a flux level equivalent to that of the highest spatial frequency sampled, i.e., 5.5 cycles arcsec^{-1}. Note that the seeing-dominated spatial frequencies were not fitted. The results of least-squares fitting of these models are shown in Table 1, and the azimuthal averages and cuts are also shown in Figure 1. Also plotted in Figure 1 are data obtained by D. McCarthy (1991, private communication) with a slit-scanning one-dimensional system at both the Mayall 4 m and the Steward Observatory 2.3 m at 3.5 μm. The uncertainty in these data is

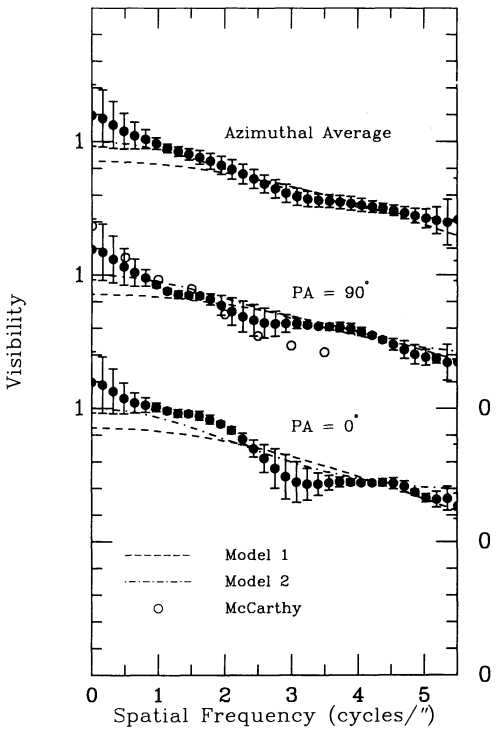

FIG. 1.—Azimuthal average and north-south and east-west cuts through the final BN visibility compared to two Gaussian distributions, and also to McCarthy's one-dimensional data. The visibilities have been arbitrarily normalized to set the zero spatial frequency of model 2 to unity.

~5%, so that the two curves essentially overlap. The second model shows better agreement with the data. However, in the absence of higher spatial-frequency components, the two models represent only two interpretations of the limits on the shell size—a more physical model, below, will give a more likely physical size. Investigation of the recovered Fourier phases showed no structure, implying the object to be *symmetric*.

3.3. *A Radiative Model*

This visibility measurement of BN contains comparatively little intrinsic information content, since the source is not even resolved (in the classical sense). However, use of ancillary information will allow us to draw reasonable and testable conjectures concerning the source structure and a corresponding value of its size, as constrained by the visibility. In order to interpret the visibility, we will propose an empirical model, intended to be the simplest which accounts for the observational data, with a minimum of additional assumptions.

The simplest structure consistent with the spectrum is a star surrounded by a dust shell. We do not know the geometry of this shell. The extinction in the line of sight to the star may be

TABLE 1

GAUSSIAN MODEL FITS TO VISIBILITIES SHOWN IN FIGURE 1[a]

Model Number	Stellar Flux (%)	Shell (%)	σ (Major Axis)	σ (Minor Axis)	P.A.
1.....	0	100	0″.037	0″.032	18°
2.....	68	32	0.112	0.086	26

[a] Note elliptical Gaussian of the form $g(r) = A \exp[-(r/\sigma)^2]$.

inferred from the reddening observed in the H II emission which is associated with the star (Scoville et al. 1983). The extinction is approximately $A(3.6\ \mu m) = 0.84$ mag. We cannot be certain how to allocate this between the shell and the foreground molecular cloud. However, H_2 emission at various locations near BN shows extinction $A(3.6\ \mu m)$ in the range from less than 0.4 to 1.0 mag (Scoville et al. 1982). We will consider two cases: first, assuming all of the extinction is in the circumstellar shell, and, second, assuming this extinction is equally divided between the shell and the foreground cloud.

The luminosity of the central star is not certain. We will explore two cases for the stellar luminosity. First, we assume that the star is sufficiently luminous, $1.5 \times 10^4\ L_\odot$, to provide the UV excitation implied by the H II emission (Scoville et al. 1983). However, as is often true of hot young stellar objects (YSOs), this implied luminosity is greater than can be verified from the total apparent bolometric luminosity of the source. Therefore, we also consider the case of a stellar luminosity matched to the observed BN luminosity, $1.5 \times 10^3\ L_\odot$. These two cases correspond to ZAMS stars of type B0.5 ($T_{\rm eff}$ = 26,000 K) and B3 ($T_{\rm eff}$ = 18,000 K) (Panagia 1973).

The spectrum of the infrared excess is adequately represented by optically thick emission at a radiation temperature of 530 K (Becklin, Neugebauer, & Wynn-Williams 1973). A decomposition of the spectral energy distribution satisfying these conditions is shown in Figure 2, based on an extinction law $A \propto \lambda^{-1.7}$. The two distributions for the shell flux differ slightly depending on whether or not part of the extinction is foreground, as mentioned above. In either case, the shell absorbs more than 99% of the stellar flux.

The two reddened stellar energy distributions correspond to the two assumed stellar luminosities. They are independent of the location of the extinction. The higher flux level curve corresponds to the lower luminosity case ($T_{\rm eff}$ = 16,000 K). The absorbed flux is assumed to be reradiated in the shell. This case corresponds to the assumption of a spherically symmetric shell. The lower flux curve corresponds to the high-luminosity case ($T_{\rm eff}$ = 26,000 K). It is lower here because, with the higher temperature, a greater proportion of the flux is emitted in the UV. In this case, the shell emission amounts to only 10% of the absorbed stellar flux, indicating a nonspherical star or envelope.

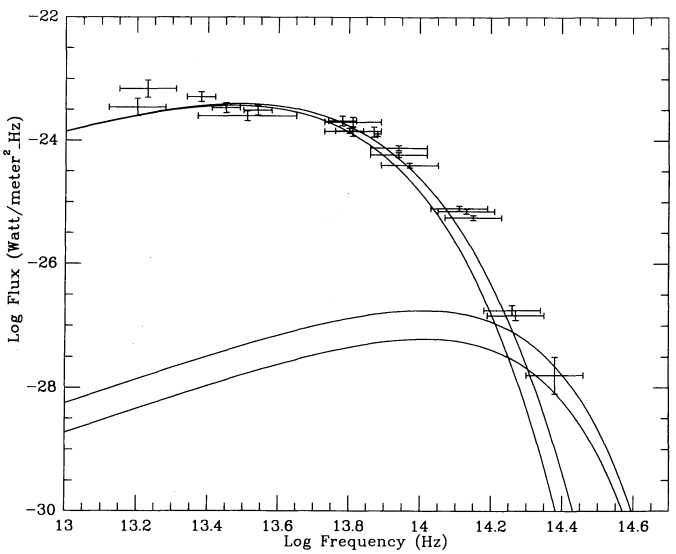

FIG. 2.—Proposed decomposition of the spectral energy distribution of the BN object superposed on photometric measurements.

The photometry shown in Figure 2 is, with several exceptions, taken from the literature (Becklin et al. 1973; Ney, Strecker, & Gehrz 1973; Dyck & Howell 1982; Simon, Simon, & Joyce 1979; Smith, Larson, & Fink 1979; Low et al. 1970). Additional unpublished *HKLMN* photometry was kindly provided by R. Joyce. Finally, M. Merrill (1991, private communication) derived a *J*-magnitude of 12.6 from an image of the Orion region; the conservative error estimate takes into account substantial uncertainty due to structure in the region's extended emission. Note that the horizontal "error" bars show filter width rather than error.

The decomposition of flux in Figure 2 indicates that BN will be dominated by the shell at all wavelengths for which infrared spatial information is available ($\geq 2.2\ \mu m$). This prediction is not strongly dependent on the uncertainties in Stellar luminosity and proportion of foreground extinction. However, it is strongly dependent on the assumption of the spherical geometry. Thus, if the dust geometry were disklike, the proportion of stellar flux could be greater or less if our radial direction from the star contained more or less extinction than average. This condition is testable. The actual BN flux distribution in the 1–1.5 μm region can be examined for consistency with the model The single measurement at 1.25 μm indicates that the stellar flux fraction is certainly not higher than the model predicts, and in fact is consistent with a spherical shell surrounding a spherical B3 star (suggesting that any disk does not introduce large asymmetry in emission of stellar radiation).

The variation of the visibility with wavelength can be examined for consistency with the model. On the blue side of the stellar/shell crossover, the visibility should reflect an unresolved rather than a partially resolved source. The approximately constant visibility function to the shortest wavelengths yet observed (2.2 μm) shows that the stellar flux fraction is small at these wavelengths.

In order to interpret the visibility measurement, we have adopted an empirical model of the dust shell, as described by Ridgway et al. (1986). Such a model captures the essential features associated with the geometry and the variation of Planckian emission with temperature. The parameters and assumptions are summarized in Table 2. The interpretation of the visibility will depend primarily on the assumed spherical symmetry and secondarily on the optical thickness, for which the two cases are shown. Dependence on other assumptions is weak. The radial intensity distribution is shown in Figure 3. The curves show the familiar shape of a shell with intermediate optical thickness. The thicker shell (*upper curve*) corresponds to the case in which all of the observed extinction is circumstellar, and the lower curve corresponds to the case in which the extinction is equally divided between the shell and foreground cloud. The emission from the inner boundary of the dust shell, at the impact parameter corresponding to the radius, provides a sharp peak in the intensity, showing that the apparent size of the shell is dominated by the inner diameter rather than by the "outer" diameter. (Note that the stellar surface intensity is very large in the arbitrary units of Figure 3. Nevertheless, with the appropriate spatial weighting, the star contributes negligibly to the total flux and hence to the visibility function.) The analysis of the visibility data proceeds by computing the visibility functions of the distributions in Figure 3, with the apparent angular scale as the free parameter. The observed BN

TABLE 2

PARAMETERS OF RADIATIVE TRANSFER MODELS

T_{eff} (K)	R_{in}	T_{in} (K)	$n_d(r)$	$T_d(r)$	τ
18,000.....	1153 R_*, 0.″05	530	r^{-2}	$r^{-0.5}$	0.42, 0.84
26,000.....	2400 R_*, 0.″05	530	r^{-2}	$r^{-0.5}$	0.42, 0.84

visibility constrains the apparent angular diameter of the inner dust envelope boundary in the model to be 0.″1 ± 0.″02. Note that our radiative model predicts a flux distribution very similar to a uniform disk with the same diameter as the inner diameter of the model envelope. By contrast, the Gaussian distribution discussed earlier is not very suitable.

The model visibility curves are plotted with the azimuthal average visibility data in Figure 4. In addition to the radiative models described above, Figure 4 includes a visibility curve for a uniform-temperature model which might be applicable to the case of mass loss (White & Becker 1982). For this model the observations require a diameter at optical depth unity of 0.″09. The similarity of the five model curves in Figures 1 and 4 show that partially resolved data such as these do not discriminate well among alternative intensity distributions.

This envelope diameter may be compared with other measures of the envelope and circumstellar region. BN has been previously observed with one-dimensional IR speckle cameras at a number of different wavelengths (Foy et al. 1979 and Chelli, Léna, & Sibille 1979 at 3.5 and 4.8 μm; and Dyck & Howell 1982 at 4.8 μm). The 1979 observations report that at 3.5 μm the BN object is barely resolved and a uniform disk diameter of 0.″08 is estimated. At 4.8 μm the diameter is estimated at 0.″1. Dyck & Howell estimate a 0.″08 uniform disk diameter.

The radiometric envelope diameter, implied by the observed color temperature and flux, is 0.″062 for optically thick emission. The models in Figure 3 would give radiometric diameters of 0.″075–0.″08 (from the spatially weighted intensity mean), in reasonable consistency considering the loose definition of the color temperature. Models for the radio emission (Moran et al. 1983) indicate a possible diameter for the H II region of 0.″06–0.″09, consistent with and comfortably inside the measured dust shell inner diameter.

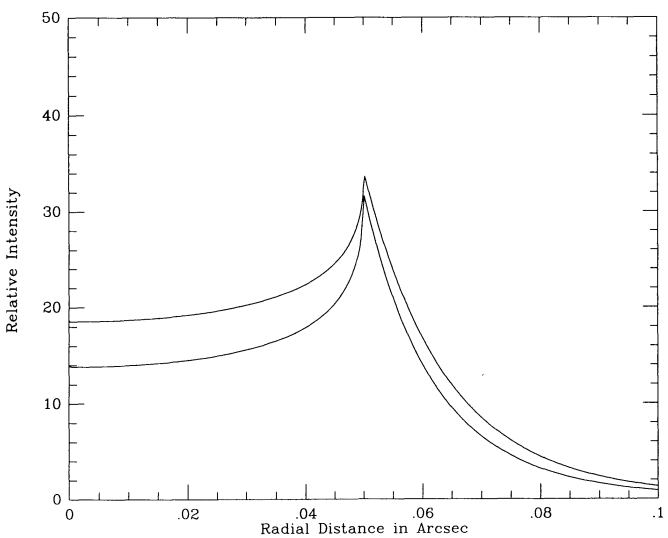

FIG. 3.—Radial intensity distributions at 3.6 μm for the two spherically symmetric shell models described in Table 2.

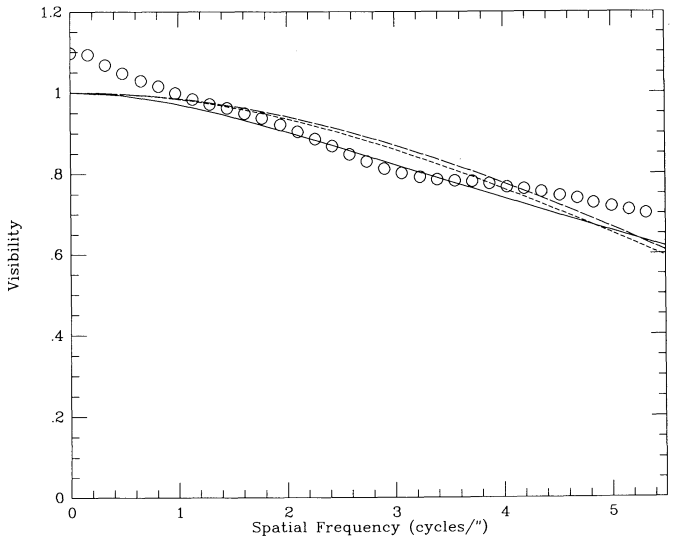

FIG. 4.—BN azimuthal average visibility, with three models. *Short-dashed line:* T_{eff} = 18,000 K model; *long-dashed line:* T_{eff} = 26,000 K model; *solid line:* uniform-temperature model.

In summary, the data presented here support the earlier result that the BN object is partially resolved. They give important spatial frequency coverage, out to 5.5 cycles arcsec^{-1}, compared to 3.5 cycles arcsec^{-1} for the earlier measurements. This is not sufficient to determine the nature of the object uniquely, making it a prime candidate for future long-baseline studies. However, the hypothesis of a spherical dust shell of intermediate thickness surrounding a B3 ZAMS star appears consistent with the photometric and spatial measurements. This simple model suggests several testable predictions. First, the stellar flux should be detected photometrically at wavelengths shorter than about 1.6 μm. Second, the circumstellar shell should be fully resolved at 3.8 μm with a telescope aperture or interferometric baseline of about 8 m. Third, the spatial visibility at low spatial frequencies at 1.6 μm and shorter wavelengths should be substantially reduced relative to the observed values at 2–5 μm.

4. IRc2 AND ITS SURROUNDINGS

4.1. *Data Analysis*

This section extends a preliminary note (Dougados et al. 1990) which reported just the 1989 November observations. The astrometric results have changed slightly owing to subsequently improved parameters for the spatial scale calibration binaries.

4.1.1. *Wide-Field Map at L′*

A wide-field map with pixel sampling of 0.″25 of the inner 30″ of the BN-KL nebula at L' (λ = 3.8 μm, $\Delta\lambda$ = 0.6 μm) is presented in Figures 5 (*contour plot*) and 6 (*image*; Plate 14). This composite frame is a mosaic made from four images, the result of a shift-and-add process of 500 individual frames, and is, to our knowledge, the highest angular resolution map at this wavelength (the FHWM of unresolved sources is 0.″5). The BN object is saturated in order to show the low brightness sources present. The jetlike features (0.03% of the BN maximum)

PLATE 14

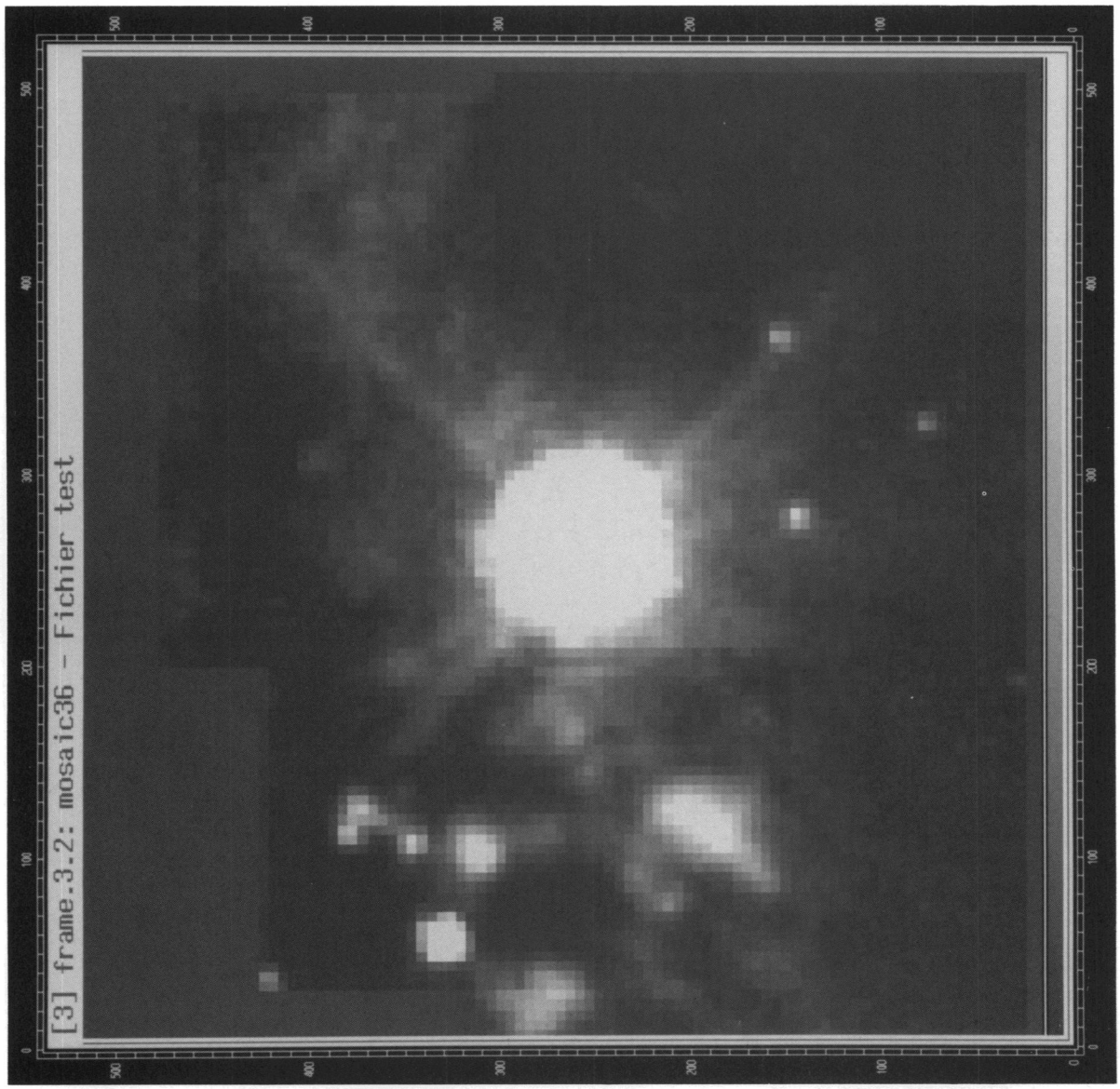

FIG. 6.—Composite of four maps of the BN-KL region at 3.8 μm, each one the result of the shift-and-add process for 500 frames. This image corresponds to the contour diagram in Fig. 5. Sources BN and *n* are strongly saturated.

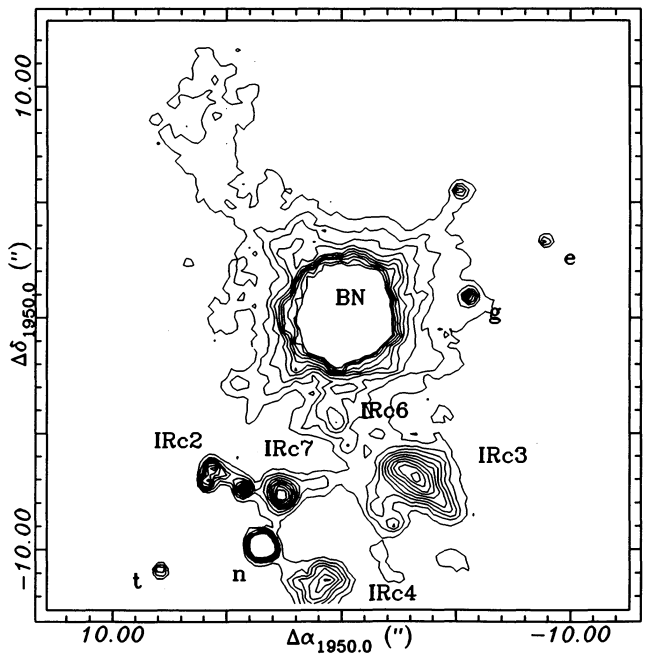

FIG. 5.—Flux levels are normalized to the BN maximum (1 unit = 13.9 Jy beam^{-1}). Pixel size is 0".2515. FWHM of pointlike sources is 0".5. Contour levels are −0.0028, 0.00025, 0.00047, 0.00069, 0.00091, 0.0011, 0.0013, 0.0016, 0.0018, 0.0020.

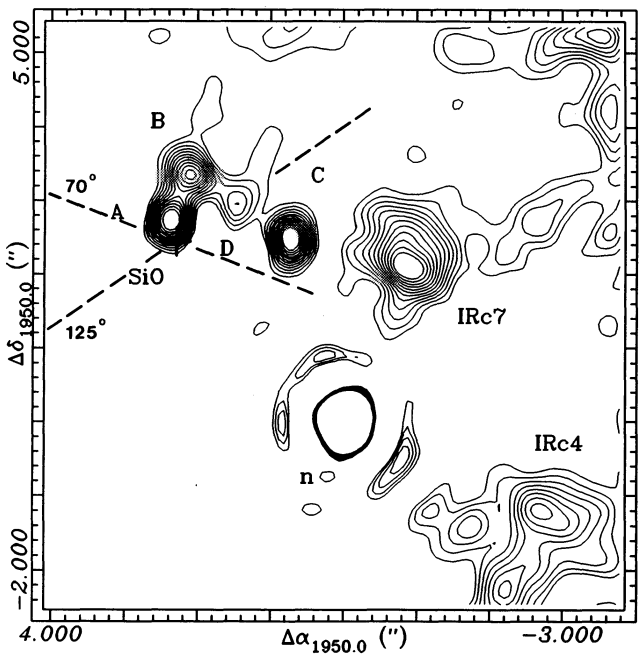

FIG. 7.—Result of the deconvolution frame-by-frame and shift-and-add of 500 individual frames using BN as a deconvolution key at 3.8 μm. The principal solution has been apodized using a Hanning filter. FWHM of source *n* on this map is 0".45. Spatial offsets are expressed with reference to source *n*. Flux levels are normalized to the peak value of source *n*. The center position of the SiO maser position (from Wright et al. 1990) is also represented, along with its error bars as well as the axis of symmetry of the low (P.A. 70°) and high (P.A. 125°) molecular outflows (*dashed lines*) associated with IRc2. Contour levels are −0.11, 0.00, 0.0078, 0.016, 0.023, 0.031, 0.039, 0.047, 0.054, 0.062, 0.070.

apparent at P.A. 45°, 135°, and 315° are artifacts due to diffraction from the spider of the telescope, as has been checked on a reference star. They show the large dynamic range of the camera ($>10^4$). However, the bright jet to the northeast appears larger than the diffraction spikes observed on a calibration star, and coincides with a previously noticed nebulosity, which has been shown to be highly polarized in the near-infrared (Minchin et al. 1991; Werner et al. 1983)—consistent with BN being the source of illumination. The map presents some interesting characteristics, the most prominent being the confirmation of the *asymmetric structure of IRc2*, resolved in three components (which we propose to name A, B, and C).

4.1.2. *Deconvolved Maps*

Figure 7 is a high-resolution map at *L'* centered on IRc2 obtained by deconvolving frame by frame a set of 500 individual images, using BN as a deconvolution key. We believe that this is the first time that *speckle holography* (Bates, Gough, & Napier 1973) has been used in the infrared. The principal solution, obtained by inverse Fourier transform has been apodized using a Hanning filter. This procedure slightly degrades the resolution but enhances the signal-to-noise ratio. As expected, the deconvolved map removes a slight residual astigmatism (probably arising in the telescope optics) and shows an improvement on angular resolution as compared with the shift-and-add map. Moreover, the deconvolved map reveals a new component in the IRc2 complex, IRc2-D. This method has been also applied at 4 and 5 μm; the results are presented in Figure 8.

4.1.3. *Polarimetric Map at L'*

Speckle polarimetric observations were also performed in 1989 November. A linear wire-grid polarizer was inserted in the optical beam before the Dewar. Four position angles were

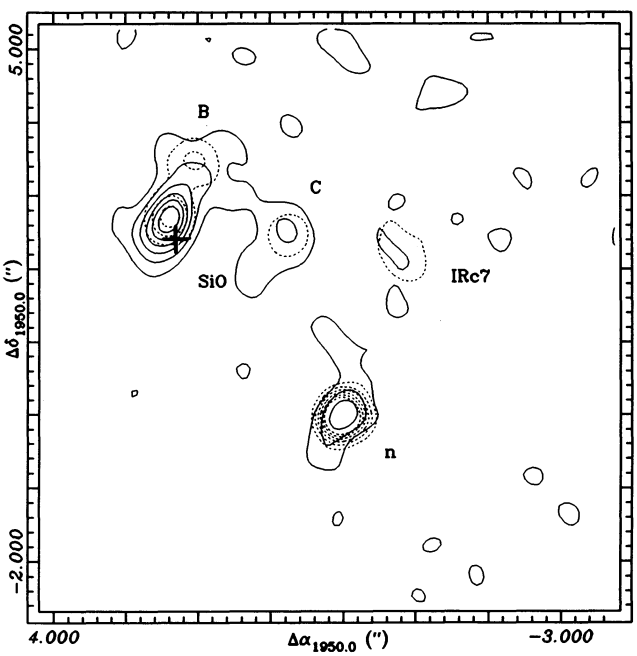

FIG. 8.—Result of the frame-by-frame deconvolution at 5 μm (*solid lines*), apodized solution. For comparison the map obtained at 4 μm is superposed, using the same reduction procedure (*dotted lines*). Note the predominance of IRc2-A at long wavelengths. Flux levels are normalized on the peak emission level of source *n* at 4 μm and of IRc2-A at 5 μm. The position of the centroid of the SiO maser emission is also reported. Contour levels are −0.29, 0.1, 0.25, 0.40, 0.55, 0.70, 0.85, 1.0.

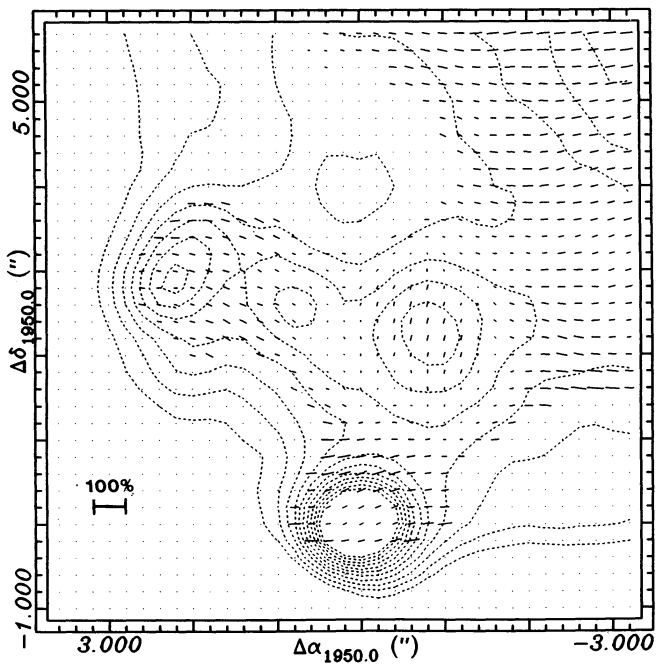

FIG. 9.—Polarization map at L' in the vicinity of IRc2, obtained using a speckle technique. Points with signal-to-noise ratio less than 5 have been masked. The distance between two pixels corresponds to a degree of polarization of 50%. The brightness distribution at L' is also represented (*dotted lines*).

used (0°, 45°, 90°, and 135°). For a given angle, 500 individual speckle frames were re-centered and co-added. The resulting polarimetric map is presented in Figure 9. Table 3 summarizes the integrated polarization values corresponding to the main infrared sources. Numerical integration has been performed in diaphragms of suitable radius centered on the source. Points with signal-to-noise ratio less than 3 have been excluded.

Our observations compare well with those of Minchin et al. (1991) for BN and IRc7. There is, however, a significant difference in the integrated polarization values of sources *n* and IRc2. In both cases, this discrepancy could be explained by our better angular resolution. The polarization map shows that important variations of the polarization vector take place in the vicinity of these sources. The effect of low angular resolution is to average these variations and thus considerably affect the determination of the polarization. The IRc7 source is less sensitive to such an effect, because it is distinct from its environment. Our integrated polarization value on BN itself is lower than previous determined values. This could result from the influence of the extended emission component (highly polarized at 3.8 μm; Werner et al. 1983) and our reduced integration diaphragm.

The degree of linear polarization in the vicinity of sources IRc2–IRc7 never exceeds 30% and lies mainly around 15%. This value is significantly lower than the 50% level observed for the extended emission component (Werner et al. 1983). The core of IRc7 and source IRc2-C have polarization values of the order of 10%, while IRc2-A, B and source *n* are polarized at $\simeq 15\%$.

4.1.4. *Photometric Calibration*

Fluxes have been calibrated using spectral observations of BN by Aitken et al. (1981). The photometry given in Table 4 corresponds to numerical integration in diaphragms centered on the source, adjusted so that contamination by neighboring sources is negligible. Points with signal-to-noise ratio less than 2 have been excluded. The extended emission component has not been subtracted. The photometry of sources IRc2-A, B, C, D and IRc7 has been obtained on the deconvolved maps, using source *n* as a photometric reference. No reliable photometry could be derived at 5 μm because of problems in sky cancellation. The uncertainties on the given values are $\leq 20\%$.

Our observed flux density at 3.8 μm for the IRc2 complex (sum of the four components) is 0.48 Jy (magnitude of 6.9 ± 0.3). This is an order of magnitude less than the value of 4.8 Jy derived by Aitken et al. (1981) in a 3".4 diaphragm and a factor of 2 less than the 0.87 Jy observed by Wynn-Williams et al. (1984) in a 2" diaphragm. It compares well with the magnitude of 7 ± 0.3 at 3.6 μm given by Minchin et al. (1991) in a 2" diaphragm. The discrepancy with earlier observations could be due to a better angular resolution which helps avoid contamination by extended background emission or neighboring sources. This stresses the importance of high angular resolution for accurate photometry in such crowded fields.

4.1.5. *Astrometry*

For pointlike sources, the astrometry has been determined with respect to BN on the shift-and-add map. First, the array pixel scale and orientation on the sky were calibrated from γ Ari, the orbital elements of which were independently determined (Dahn 1990) to be

$$\text{Separation} = 7''.615 \pm 0''.004\,, \quad \text{P.A.} = 0°.49 \pm 0°.04\,,$$

$$\text{JD} = 2{,}448{,}192.7782\,,$$

giving a calibration scale of $0''.2515 \pm 0''.0002$ pixel^{-1} and 0°.00

TABLE 3

INTEGRATED POLARIMETRIC OBSERVATIONS AT 3.8 μm OF THE BN-KL NEBULA

	WERNER ET AL. 1983			MINCHIN ET AL. 1991			OUR OBSERVATIONS		
SOURCE	ϕ	P (%)	θ	ϕ	P (%)	θ	ϕ	P (%)	θ (°)
BN	6"	8.4 ± 1.0	177°	6"	8.5 ± 0.3	117°	2.4	6.6 ± 0.3	118°.8 ± 1°.5
Source *n*	...	...	...	3	4.2 ± 0.5	144 ± 8°	0.8	16.6 ± 1.2	110 ± 2
				...	...	...	0.2	12.6 ± 4	115 ± 8
IRc7	...	...	...	2	7.5 ± 1.5	175 ± 9	2	7.5 ± 14	171 ± 55
							0.8	14 ± 14	168 ± 30
IRc2	6	10.5	167	2	3.9 ± 1.0	135 ± 20	...	...	...
IRc2-A	...	...	...	...	...	...	1.2	14 ± 1	79.5 ± 2.5
IRc2-B	...	...	...	...	...	...	1.2	17 ± 4	81.5 ± 7
IRc2-C	...	...	...	...	...	...	1.2	8.3 ± 11	61 ± 37

$\pm$ 0.″06 relative rotation. Second, the offsets were measured from BN using the center of gravity of a box of 5 pixels (unresolved sources) or 3 pixels (extended objects) centered on the brightest pixel. The accuracy of this positioning is of the order of 0.1 pixel. Third, we assume the BN radio continuum position (Moran et al. 1983) to coincide with the L' peak intensity, a satisfactory assumption for an ultracompact H II region confined within a dust cocoon of size $\approx$0.″1 emitting at L', as established above.

Additional possible uncertainties in our procedure, which have been considered, are the following:

1. The influence of anisoplanetism on an angular distance of $\approx$9″ (BN-IRc2 separation), causing an intrinsic dispersion in the measured distance around the true value. Such an effect has been evaluated by measuring the dispersion of the distance between the two components of the calibration double star γ Ari for 500 individual frames. The resultant dispersion in distance on the final shift-and-add image has been found to be less than 0.01 pixel.

2. The difference in colors between the calibration double star and the object causes a shift in effective wavelength, hence a slight difference in the pixel scale calibration. From the shape of the L' filter and the estimated wavelength dependence of the brightness of both the object and the double star, we estimate the shift in effective wavelength between BN and γ Ari to be 0.08 μm. The color dependence of the pixel scale calibrated on γ Ari gives a mean slope of 0.2% μm^{-1} near 3.8 μm. The resulting difference in pixel spatial calibration is 4×10^{-5} μm—well within the error bars.

3. The uncertainties on the determination of the separation and position angle of the calibration double star, due to atmospheric refraction, have been also estimated. They are less than 0.″002 for the separation and 0.°3 for the position angle, significantly less than the error bars. Moreover, on the field of the camera (typically the distance between BN and IRc2), the uncertainties on $\Delta\alpha$ and $\Delta\delta$ are of the order of 0.″005.

The above three sources of uncertainties are thus negligible compared with the error bars associated with the BN radio continuum position and have not been corrected. For the unresolved sources on the shift-and-add map, the uncertainties in the derived offsets from the BN position are $\leq$0.″05. The error bars in the astrometry of such sources are then dominated by the errors of the radio BN position ($\Delta\alpha_{1950.0}$ = 0.″15, $\Delta\delta_{1950.0}$ = 0.″1; Moran et al. 1983). The objects IRc2-A, B, C, D and IRc7 have been positioned with respect to source *n* on the deconvolved map (principal solution). The astrometry of source *n* is accurately derived from BN as established above. For IRc2-C the error in the positioning with respect to source *n* is of the order of 0.″05. For the other sources the astrometric accuracy is essentially limited by the resolution. The absolute positions of the sources presented in Table 4 are compatible within the error bars of earlier results of McCaughrean (1988).

The photometric and astrometric results are summarized in Table 4. Sources are named according to Downes et al. (1981) and Lonsdale et al. (1982).

4.2. *Main Results*

The prominent new results concerning the main infrared sources are detailed below.

IRc2.—The IRc2 object is resolved into four components: A and B, discovered by Chelli et al. (1984) using one-dimensional speckle observations, C (unresolved), and an additional faint pointlike object (D) which manifests itself as an extension toward the west of IRc2-B on the shift-and-add map but is clearly resolved on the deconvolved map. A northwest-elongated structure, jetlike, originates near IRc2-D (it is already suggested on the shift-and-add map). The two components IRc2-A and IRc2-B show the *double-peaked morphological structure* initially assumed to fit the doughnut geometry proposed for the SiO maser emission (Plambeck et al. 1990). They are essentially unresolved although component B appears slightly *fan-shaped.* The distance between IRc2-A and IRc2-B, determined on the deconvolved map, is 0.″68 $\pm$ 0.″05 (350 AU at 480 pc) with P.A. 155° $\pm$ 5°. The three components A, B, and C are also detected at 5 μm, A becoming more

TABLE 4

SUMMARY OF PHOTOMETRIC AND POLARIMETRIC OBSERVATIONS OF MAIN INFRARED SOURCES IN THE BN-KL NEBULA

SOURCE NAME	$\alpha_{1950.0}$ ($\pm$0.″15)	$\delta_{1950.0}$ ($\pm$0.″1)	FWHM		F_ν (Jy)		NOTES
			Shift-and-Add	Principal Solution	L'	L''	
BN	05:32:46.640	−05:24:16.45	0.″5	...	100	124	Unresolved
n	05:32:46.874	−05:24:26.31	0.5	0.″3	1.54	1.31	Unresolved
g	05:32:46.272	−05:24:15.53	0.5	...	0.17	0.94	Unresolved
e	05:32:46.048	−05:24:13.12	0.5	...	0.03	...	Unresolved
t	05:32:47.169	−05:24:27.34	0.5	...	0.04	...	Unresolved
aa	05:32:46.297	−05:24:10.99	0.5	...	0.12	...	Unresolved
IRc3	05:32:46.423	−05:24:23.47	...	...	2.61	1.66	Extended
IRc6	05:32:46.658	−05:24:20.97	0.8	...	0.23	0.25	Nebulous
IRc2-A	05:32:47.030	−05:24:23.66	0.7	0.4	0.14	0.37	Unresolved
IRc2-B	05:32:47.013	−05:24:32.02	0.8	0.4	0.12	0.26	Unresolved
IRc2-D	05:32:46.975	−05:24:23.41	...	0.4	0.06	0.09	Unresolved
IRc2-C	05:32:46.924	−05:24:23.85	0.5	0.3	0.16	0.26	Unresolved
IRc7	05:32:46.823	−05:24:24.28	1.0	0.4	0.53	0.62	Extended

NOTE.—The astrometry of BN corresponds to the radio continuum position (Moran et al. 1983). The astrometry has been determined on the L' shift-and-add map, except for the IRc2 components and IRc7, for which it has been derived from the deconvolved L' map, using source *n* as the astrometric reference. The first number in the FWHM column corresponds to the shift-and-add L' map, while the second one (when present) refers to the deconvolved L' map (principal solution). The flux densities correspond to numerical integration in the beam of diameter 3 × FWHM, performed on the shift-and-add maps, except for the IRc2 components and IRc7, for which the photometry has been calculated on the deconvolved maps (source *n* being the photometric reference). The flux densities have been calibrated on the spectral observations of BN by Aitken et al. 1981.

prominent at that wavelength. Recently Gezari (1992) performed high angular resolution imaging at 8.7 and 12.3 μm of the BN-KL nebula. Accurate astrometry ($\Delta\alpha = \Delta\delta = 0\farcs2$) has also been obtained by this author, thus enabling comparison with our observations. The peak of emission toward IRc2 at 8.7 and 12.4 μm appears to register spatially with our B component. No emission is detected toward IRc2-A at these wavelengths. An extended structure, elongated along the B/C direction, is also observed.

IRc3.—The IRc3 source has been resolved by Minchin et al. (1991) in two components: i_1 (southeastern lobe) faint but detected at J, and i_2 (northwestern lobe) appearing at H and prominent at K and L. Polarimetric observations by Minchin et al. (1991) show that the source is highly polarized at H, K, and L (10%, 13%, and 35%, respectively) with a position angle consistent with IRc2 being the source of illumination. The object disappears at intermediate wavelengths (5–12 μm) but becomes visible again at longer wavelengths (>20 μm). Our observations at 3.8 μm show the elongated structure (along P.A. 45°, east from north) of the i_2 lobe and resolve i_1 into two pointlike condensations.

IRc4.—IRc4 shares many of the observational characteristics of IRc3 (high degree of linear polarization in the near-infrared, silicate band seen in absorption, disappearance at intermediate wavelengths). This source also spatially coincides with low-velocity H_2O maser emission (Downes et al. 1981). On our 3.8 μm maps, it appears extended and elongated along P.A. 150°. A ridge of emission links it to source *n*. It is not detected at 5 μm. Its proximity with the edge of the camera field of view made the determination of its photometry and polarimetry impossible.

IRc6.—IRc6 is now part of a BN "finger" pointing toward the south, distinct from the spider artifacts. It is detected in our observations at 5 μm. It is also observed at 12.4 μm (Gezari, Folz, & Woods 1989) and 20 μm (Downes et al. 1981). Its proximity to BN makes difficult the determination of its photometry and polarimetry.

IRc7.—The IRc7 object has been previously detected at K and L (Minchin et al. 1991), at 12.4 μm (Gezari et al. 1989) as well as at 20 μm (Downes et al. 1981). It appears extended and nebulous on our L' shift-and-add map (FWHM = 1″). The deconvolved L' map (principal solution) shows an essentially unresolved component (FWHM = 0″.4) embedded in a nebulosity. It is not detected at 5 μm. The polarimetric observations at L' show a polarized core (14%) surrounded by a depolarized ring (a few percent). The transition occurs at roughly 1″.4 from the central emission peak. Simultaneously the angle position of the polarization vector rotates by 90°.

Source n.—Source *n* is detected and unresolved at all our observed wavelengths. Relatively faint at H and K, it becomes prominent at L' (Lonsdale et al. 1982). It shows also on the infrared map of Gezari (1992) at 8.7 μm but is not detected by this author at 12.4 μm. It has no association with a visible star. Gezari (1992) reports that source *n* coincides with a new 22 GHz radio source detected by Merten & Reid (1991).

Other sources.—A ring of emission, centered on a dark area corresponding to a maximum of density of the molecular cloud, links IRc4, IRc7, IRc3, and source *n*. Three unresolved objects (FWHM = 0″.5) correspond to sources *e*, *g*, and *t* of Lonsdale et al. (1982). They are associated with the visible stars π1820, π1821, and π1839, respectively. A fourth pointlike source appears to the north of source *g*, which we propose to call source *aa* following the nomenclature of Lonsdale et al. (1982). It has no association with any of Lonsdale's sources but is present on the L map of Minchin et al. (1991).

Some conclusions may be derived from the observations of these sources:

1. IRc3, IRc4, and IRc7 share the same observational characteristics: they are all resolved, undetected at intermediate wavelengths (5 μm) but show up again at longer wavelengths (>10 μm, Gezari 1992). This is consistent with the earlier interpretation (Downes et al. 1981, Minchin et al. 1991) of the sources being dust density enhancements reprocessing the light of another object, while our measured polarization of IRc7 indicates IRc2 as a possible illuminating source.
2. Source *n* remains unresolved at all wavelengths and still prominent at 5 μm, consistent with its identification as a reddened star (Lonsdale et al. 1982). Additional photometry on a broader spectral range is needed to establish the foreground extinction and decide whether this pure infrared source is part of the BN-KL nebula, as has been suggested by Lonsdale et al. (1982), or a reddened Trapezium cluster young star (Wynn-Williams et al. 1984; Minchin et al. 1991). Its association with a new compact radio source, however, makes it a good candidate for an embedded young stellar object.
3. IRc2 appears extremely complex and will be discussed below.

4.3. *Discussion: The Nature of the IRc2 Complex*

IRc2 has been previously understood as a single bright object providing, with BN, most of the luminosity reradiated in the infrared, and associated with high-velocity molecular flows and with H_2O and SiO maser emission. Our high-resolution observations show the complex structure of IRc2 and raise questions about this simple picture.

Of particular interest is the position of the infrared source IRc2 with respect to the radio sources (H_2O and SiO masers, radio continuum sources). This determination is essential to understanding the exact nature of IRc2 and its role in the energetics and flow properties of this complex region. Thanks to our accurate astrometric calibration, we are able to position the centroid of the SiO maser emission ($5^h32^m47\overset{s}{.}026 \pm 0\overset{s}{.}01$, $-5°24'23\farcs88 \pm 0\farcs2$; Wright et al. 1990) on the deconvolved 3.8 μm map (Fig. 7), using our observed position of source *n* as astrometric reference (see Table 4). The errors are dominated by the uncertainty in the relative radio (BN continuum) and microwave (SiO maser) coordinate systems. Given these uncertainties, *IRc2-A may coincide with the centroid of the* SiO *maser emission.* The maser is definitely not located on the center of symmetry between IRc2-A and IRc2-B. It should also be noted that the positions of the continuum 15 and 5 GHz emissions, characteristic of the presence of a compact H II region, lie within the error bars of the SiO maser position. Our result is confirmed by the analysis of Gezari (1992), who locates the SiO maser on his 12.4 μm map and finds it lying southeast of the IRc2 emission peak but within the error bars of the 3.8 μm IRc2-A component.

Concerning the link of the infrared source IRc2-A/IRc2-B with the molecular flows which originate near IRc2, Table 5 summarizes the observed axes of symmetry. We first note that the IRC2-A/IRc2-B long axis lies at position angle 155°, which compares well with the orthogonal axis of the low-velocity molecular flows (SiO and H_2O maser emissions, SO expanding ring), $\simeq$145°–170°, as well as of the 12.5 μm elongated emission (P.A. 170°), which probe regions close to the central object

TABLE 5

AXIS OF SYMMETRY OF THE DIFFERENT FLOWS OBSERVED ORIGINATING NEAR IRc2

Source	P.A.	Size (arcsec)	Reference
⊥ SiO maser	145°	0.15	Plambeck et al. 1990
⊥ H_2O masers	150	30	Genzel et al. 1981
⊥ SO disk	170	35	Plambeck et al. 1982
⊥ 12.5 μm source	170	1 × 2	Lester et al. 1985
∥ CO bipolar flow	≃125	20–40	Erickson et al. 1982
∥ SiO bipolar flow	≃125	10	Wright et al. 1983
∥ H_2 emission	120	60	Beckwith et al. 1978
⊥ CS disk	120	120	Murata et al. 1991

NOTE.—The parallel and perpendicular signs refer to the principal axes of the elongated structure and its orthogonal, respectively. Angles are positive east from north.

(<20″). It is, however, significantly greater than the position angle of the high-velocity molecular flows (CO, SiO, H_2), ≃125°, detected at large distance from the central source, as well as from the polar axis of the large-scale molecular CS disk detected by Murata et al. (1991). If IRc2-A/IRC2-B is a bipolar source, this discrepancy could reflect a change in orientation and dynamics of the flow with distance from the central source. Indeed, Murata et al. (1991) observe that the outer part of the CS disk shows Keplerian rotation, while the inner parts ($r < 25''$) depart from it. This they interpret in terms of a change in molecular gasdynamics at the inner edge of the disk, consistent with the SO expanding ring and the proper motion of the H_2O masers. Another possibility would be that different sources contribute to the different molecular outflows. The axes of symmetry of the low- and high-velocity molecular outflows are shown in Figure 7.

The IRc2-A and IRc2-B components clearly show a *double-peaked morphological structure*, interpreted earlier (Chelli et al. 1984) as related to the doughnut, or torus, proposed for the SiO maser emission morphology (Plambeck et al. 1990). Concerning the nature of these two components three possibilities now emerge:

1. Sources A and B could be reprocessed light from two polar lobes, the torus being perpendicular to their long axis. The two lobes should then exhibit symmetrical polarization characteristics, leading to low intrinsic polarization in the mean, as observed. The association of one lobe with the SiO maser emission would however, remain to be explained.
2. The two components may be self-luminous sources, one of them (IRc2-A) more closely associated with the outflow phenomena.
3. Source A could be thermal emission from the inner dust torus and B reprocessed light from one polar lobe, the other being obscured—compatible with an inclination of the torus with respect to the line of sight of ≃45° derived for the SiO maser emission model (Plambeck et al. 1990).

Given the coincidence of IRc2-A with the centroid of the SiO maser emission, interpreted as the center of an expanding circumstellar disk, the alignment of the bipolar infrared source with the low-velocity outflows and the predominance of IRc2-A at intermediate wavelengths (see Figure 8), we would favor the third interpretation. This is also supported by the slightly lower value of polarization in the vicinity of IRc2-A. The exact direction of illumination is uncertain but compatible with IRc2-A being one of the main illuminating sources. With this interpretation, A is a star but its luminosity remains undetermined. The second possibility cannot, however, be ruled out, considering the spatial correlation of IRc2-B with the 12.4 μm emission peak (Gezari 1992), which would suggest the presence of a heating source at this position.

The nature of the other IRc2 components (C and D) remains ambiguous. The photometric analysis presented above as well as the polarization data (low polarization value of IRc2-C; polarimetric map compatible with IRc2-C being a source of illumination) suggest that one of these components at least may be self-luminous.

These observations raise doubts about the previous result that a single massive object, identified as IRc2, is the primary source of energy for the whole infrared nebula. Indeed, Chelli et al. (1984) and Wynn-Williams et al. (1984) obtained luminosity estimates for IRc2 of $(8 \pm 4) \times 10^4\ L_\odot$ and $\simeq 10^5\ L_\odot$, respectively, comparable to the total luminosity of the infrared complex: $1.2–1.5 \times 10^5\ L_\odot$ (Werner et al. 1976; Genzel & Downes 1982). These estimates were, however, derived from photometric measurements with diaphragms of the order of 2″ centered approximately on IRc2-A/IRc2-B, thus encompassing most of the IRc2 complex. Our observations show the complexity of IRc2, resolved in four pointlike sources each having a distinct behavior with wavelength (C dominates at 3.8 μm, while A dominates at 5 μm and B at 8.7 and 12.4 μm, etc.). Hence the color temperature of the ensemble cannot be interpreted as representative of an effective temperature or be assigned to a particular component. The infrared source *n* may also contribute significantly to the energy input. Clearly, extensive photometry with high angular resolution and large wavelength coverage of each IRc2 component as well as source *n* is now needed to distinguish between a single luminous source and a cluster of YSOs to power the nebula.

5. CONCLUSION

We confirm the partial resolution of the BN shell at 3.6 μm with two-dimensional speckle measurements (short exposures, diffraction-limited sampling). The data do not show any evidence of asymmetry. Based on the assumption of spherical symmetry, the reddening obtained from the spectrum of the BN H II region, and the color temperature of the IR emission, we have constructed an empirical model of the shell. The two-dimensional visibilities combined with the photometric data are compatible with a B3 ZAMS star surrounded by the spherical dust shell of apparent inner diameter 0.″1 (50 AU at 480 pc). The H II region of diameter in the range 0.″06–0.″09 is located inside the dust shell, whose location also compares with the inner rim of the neutral surrounding CO envelope located at a distance of about 20 AU from the star (Scoville et al. 1983). The improved spatial frequency coverage of our observations is, however, not sufficient to determine the nature of the object uniquely. If our model is correct, BN should be detected in direct, highly extincted starlight near 1 μm. Interferometric measurements with a baseline of at least 10 m should detect the visibility plateau from the unresolved star and help determine the fraction of direct stellar flux and thus constrain the shell optical thickness.

Images of the inner 15″ of the BN-KL nebula have been obtained at 3.6, 3.8, 4, and 5 μm. The BN source, registered simultaneously, was treated as a point source for deconvolution of the individual frames. The high angular resolution achieved (0.″5 at 3.8 μm) reveals the subarcsecond structure of

the compact infrared sources. IRc2 is resolved in four components, essentially pointlike, two of which (A and B) align along the perpendicular of the low-velocity molecular flows associated with IRc2 and show the *double-peaked morphological structure* initially assumed to fit the doughnut geometry proposed for the SiO maser emission. Accurate astrometry locates IRc2-A within the error bars of the position of the SiO maser emission centroid, suggesting a more plausible interpretation in terms of thermal emission from dust in the inner parts of the circumstellar disk surrounding a YSO. Component B would then be *scattered light* from one polar lobe. Our observations alone cannot establish the nature of the other IRc2 components (C and D). The photometric and polarimetric data suggest, however, that these sources may be self-luminous. The complex structure of IRc2 makes questionable the temperature and luminosity globally assigned to it and leaves open the question of the particular source powering the KL nebula. Higher angular resolution observations of the molecular and mid- and far-infrared emission are clearly needed to help specify the nature of the multiple infrared sources and their link with the outflows.

We are grateful to C. Dahn, who obtained on request the CCD astrometric observations of the binary systems γ Leo and γ Ari. These observations were critical for the accurate calibration of our image scale and orientation. We thank D. Gezari for discussion of his work prior to publication. The referee suggested inclusion of the uniform temperature model in the discussion of the BN source. The work was partially supported by NATO grant RG86/0080.

REFERENCES

Aitken, D. K., Roche, P. F., Spenser, P. M., & Jones, B. 1981, MNRAS, 195, 921
Bates, R. H. T., Gough, P. T., & Napier, P. J. 1973, A&A, 22, 319
Beckers, J. M., Christou, J. C., Probst, R. G., Ridgway, S. T., & von der Lühe, O. 1988, in Proc. NOAO/ESO Conf. on High-Resolution Imaging by Interferometry, ed. F. Merkle (Garching: ESO), 527
Becklin, E. E., Neugebauer, G., & Wynn-Williams, C. G. 1973, ApJ, 182, L7
Beckwith, S., Persson, S. E., Neugebauer, G., & Becklin, E. E. 1978, ApJ, 223, 464
Chelli, A., Léna, P., & Sibille, F. 1979, Nature, 278, 143
Chelli, A., Perrier, C., & Léna, P. 1984, 280, 163
Christou, J. C. 1991, Exp. Astron., 2, 27
Churchwell, E., Felli, M., Wood, D. O. S., & Massi, M. 1987, ApJ, 321, 516
Dahn, C. C. 1990, private communication
Dougados, C., Léna, P., Ridgway, S., Christou, J., & Probst, R. 1990, in ASP Conf. Ser., Vol. 14, Astrophysics with Infrared Arrays, ed. R. Elston (San Francisco: ASP), 258
Downes, D., Genzel, R., Becklin, E. E., & Wynn-Williams, C. G. 1981, ApJ, 244, 869
Dyck, H. M., & Howell, R. R. 1982, AJ, 87, 400
Erickson, N. R., Goldsmith, P. F., Snell, R. L., Berson, R. L., Huguenin, G. R., Ulrich, B. L., & Lada, C. J. 1982, ApJ, 261, L103
Foy, R., Chelli, A., Sibille, F., & Léna, P. 1979, A&A, 79, L5
Garay, G., Moran, J. M., & Haschick, A. D. 1989, ApJ, 338, 244
Garay, G., Moran, J. M., & Reid, M. J. 1987, ApJ, 314, 535
Genzel, R., & Downes, D. 1982, in Regions of Recent Star Formation, ed. R. S. Roger & P. E. Dewdney (Dordrecht: Reidel), 251
Genzel, R., Reid, M. J., Moran, J. M., & Downes, D. 1981, ApJ, 244, 884
Gezari, D. Y. 1992, ApJ, 396, L43
Gezari, D. Y., Folz, W., & Woods, L. 1989, in Proc. Third Infrared Detector Technology Workshop, ed. C. McCreight (NASA TM-102209), 267
Jones, B. F., & Walker, M. F. 1985, AJ, 90, 1320
Lester, D. F., Becklin, E. E., Genzel, R., & Wynn-Williams, C. G. 1985, AJ, 90, 2331
Lonsdale, C. J., Becklin, E. E., Lee, T. J., & Stewart, J. M. 1982, AJ, 87, 1819
Low, F. J., Johnson, H. L., Kleinmann, D. E., Latham, D. E., & Geisel, S. L. 1970, ApJ, 160, 531
Martín-Pintado, J., Rodríguez-Franco, A., & Bachiller, R. 1990, ApJ, 357, L49
McCaughrean, M. J. 1988, Ph.D. thesis, Univ. Edinburgh
Menten, K., & Reid, M. J. 1991, BAAS, 22, 4 (abstract)
Migenes, V., Johnston, K. J., Pauls, T. A., & Wilson, T. L. 1989, ApJ, 347, 294
Minchin, N. R., et al. 1991, MNRAS, 248, 715
Moran, J. M., Garay, G., Reid, M. J., Genzel, R., Wright, M. C. H., & Plambeck, R. L. 1983, ApJ, 271, L31
Murata, Y., Kawabe, R., Ishiguro, M., Hasegawa, T., & Hayashi, M. 1991, in IAU Symp. 147, Fragmentation of Molecular Clouds and Star Formation, ed. E. Falgarone, F. Boulanger, & G. Duvert (Dordrecht: Kluwer), 357
Ney, E. P., Strecker, D. W., & Gehrz, R. D. 1973, ApJ, 180, 809
Panagia, N. 1973, AJ, 78, 929
Plambeck, R. L., Wright, M. C. H., & Carlstrom, J. E. 1990, ApJ, 348, L65
Plambeck, R. L., Wright, M. C. H., Welch, W. J., Bieging, J. H., Baud, B., Ho, P. T. P., & Vogel, S. N. 1982, ApJ, 259, 617
Ridgway, S. T., Connors, D., Dainty, J. C., Joyce, R. R., & Pipher, J. L. 1986, ApJ, 302, 662
Rigaut, F., Rousset, G., Kern, P., Fontanella, J. C., Gaffard, J. P., Merkle, F., & Léna, P. 1991, A&A, 250, 280
Scoville, N. Z., Hall, D. N. B., Kleinmann, S. G., & Ridgway, S. T. 1982, ApJ, 253, 136
Scoville, N., Kleinmann, S. G., Hall, D. N. B., & Ridgway, S. T. 1983, ApJ, 275, 201
Simon, T., Simon, M., & Joyce, R. R. 1979, ApJ, 230, 127
Smith, H. A., Larson, H. P., & Fink, U. 1979, ApJ, 233, 132
Werner, M. W., Dinerstein, H. L., & Capps, R. W. 1983, ApJ, 265, L13
Werner, M. W., Gatley, I., Harper, D. A., Becklin, E. E., Loewenstein, R. F., Telesco, C. M., & Thronson, H. A. 1976, ApJ, 204, 420
White, R. L., & Becker, R. H. 1982, ApJ, 262, 657
Wright, M. C. H., Carlstrom, J. E., Plambeck, R. L., & Welch, W. J. 1990, AJ, 99, 1299
Wright, M. C. H., & Plambeck, R. L. 1983, ApJ, 267, L115
Wright, M. C. H., Plambeck, R. L., Vogel, S. N., Ho, P. T. P., & Welch, W. J. 1983, ApJ, 267, L41
Wynn-Williams, C. G., Genzel, R., Becklin, E. E., & Downes, D. 1984, ApJ, 281, 172